VTT Technical Research Centre of Finland

An atomistic simulation study of rapid solidification kinetics and crystal defects in dilute Al–Cu alloys

Haapalehto, Matias; Pinomaa, Tatu; Wang, Lei; Laukkanen, Anssi

Link to publication

Full Length Article

An atomistic simulation study of rapid solidification kinetics and crystal defects in dilute Al–Cu alloys

Matias Haapalehto [a],*, Tatu Pinomaa [a], Lei Wang [b], Anssi Laukkanen [a]

[a] *Integrated Computational Materials Engineering (ICME) group, VTT Technical Research Centre of Finland Ltd, Espoo, Finland*
[b] *Federal Institute for Materials Research and Testing (BAM), Unter den Eichen 87, 12205 Berlin, Germany*

ARTICLE INFO

ABSTRACT

Rapid solidification kinetics of dilute Al–Cu alloys is simulated using a quantum mechanics based bond-order potential (BOP), in free solidification conditions, to determine kinetic and thermodynamic properties of solidification, as well as point defects and chemical ordering of the solidified structures. We measure the anisotropic kinetic coefficient, anisotropic solid–liquid interface energy, as well as solute trapping kinetics in terms of partition coefficient versus velocity and solute drag coefficient. Furthermore, solid–liquid interface free energy and its anisotropy are measured in equilibrium simulations, showing reasonably good agreement with previous studies. We also verified the self-consistency of the MD simulations, by comparing the interfacial temperature vs. velocity to that predicted by the continuous growth model. These solid–liquid interface properties are important for quantitative parametrization of larger scale solidification modeling techniques such as phase field models. We also investigated the point defect content, local chemical ordering, and local crystalline structures in the rapidly solidified samples. We found clustering of solute with vacancies, whereas copper atoms repelled each other in these dilute alloy simulations. In addition to vacancies, a large number of interstitials were found. In solidification velocities approaching the complete solute trapping regime, we found that the vacancies and interstitials formed in conjunction, i.e. as Frenkel pairs. Finally, in addition to FCC, we detected BCC and HCP phases, where the latter two were accompanied by an increase in local copper content. Understanding the formation of point defects and their relationship to chemical ordering is an important step towards controlling the formation of pre-precipitates and precipitates, which are an important strengthening mechanism for aluminum–copper alloys.

1. Introduction

Several industrial materials processing techniques operate in rapid solidification regime, such as thermal spray coating deposition [1], certain welding techniques [2], melt spinning [3], and metal additive manufacturing [4–6]. Compared to near-equilibrium conditions, rapid solidification leads to drastically altered microstructures through selection of metastable phases [7], solute trapping kinetics [8–10], changes in solidification morphology [11], and reduction of microstructural feature sizes such as dendrite primary arm spacing [11]. Rapid solidification also increases the crystal defect content [12], for example through formation of excess vacancies [13] and high dislocation densities [14–16]. For aluminum alloys, point defects have a significant effect on chemical ordering and act as nucleation sites for Guinier–Preston zones [3], which are important to understand and control for precipitation-hardened, such as aluminum–copper, alloys [17,18]; these alloys have challenges in rapid solidification (for metal additive

manufacturing) conditions, mostly related to the control of their metallurgy, but have great potential, e.g., for transportation industry due to their high strength and low weight [6].

Computational simulations can be used to illuminate the transient and small-scale phenomena that are characteristic to rapid solidification. Microstructure evolution models, such as phase field models [19, 20], rely on determination of kinetic and thermodynamic properties of the solid–liquid interface, in particular the anisotropic kinetic coefficient, anisotropic solid–liquid interface energy, and solute trapping data. These material parameters can be readily extracted from molecular dynamics simulations [21,22], recently evaluated for example for Fe–Mn [23] and Ti–Ni alloys [24].

While in the past there have been atomistic simulations of rapid solidification for pure aluminum [13,25] and Al–Cu alloys [26–28], to our knowledge, there has not been a systematic extraction of rapid solidification kinetics parameters using a high quality Al–Cu potential.

---

* Corresponding author.
 E-mail address: matias.haapalehto@vtt.fi (M. Haapalehto).

In this paper, we carry out an atomistic investigation into rapid solidification of dilute Al–Cu alloys using a bond-order potential with an analytical form derived from quantum mechanics [29]. Firstly, we determine thermodynamic and kinetic properties of the solid–liquid interface, including solute trapping (velocity-dependent partition coefficient and solute drag analysis), anisotropic kinetic coefficient, and anisotropic solid–liquid interface energy. Secondly, we analyze the solidified Al–Cu structures in terms of point defects (vacancies and interstitials), detected crystal structures (FCC vs. BCC vs. HCP), and the relationship of these structural features to the local chemical (copper) ordering.

2. Methods

2.1. Bond-order potential

Simulations are performed using the LAMMPS classical molecular dynamics code distributed by Sandia National Laboratories [30]. Interatomic interactions are described using an analytical bond-order potential (BOP) developed by Zhou et al. [29]. The BOP has been derived from quantum mechanical principles and offers several advantages for this work, such as a good description of the melting temperature and defect characteristics [29].

2.2. Evaluation of phase diagram properties

Equilibrium calculations were performed with two purposes in mind. Firstly, the results give an indication of the quality of the potential in terms of reproducing the true phase diagram, which is one of the fundamental material properties controlling its solidification behavior. Secondly, the equilibrium calculations allow us to precisely control the solidification driving force, and therefore, the solidification velocity. This is achieved by adjusting the temperature and the composition of the system relative to the known equilibrium solidus and liquidus points measured from MD.

Solidus and liquidus points were determined using semi-grand canonical MC (SGCMC) simulations following Ref. [31], and the details of this procedure are presented in the Supplementary material. The results of equilibrium calculations are shown in Fig. 1 along with a reference phase diagram generated using Thermo-Calc (TCAL6 database). The potential slightly overestimates the pure material melting point. The solidus concentration at $T = 900$ K predicted by the potential is slightly larger, and the liquidus concentration is slightly smaller, compared to the Thermo-Calc values. The phase diagram solidus and liquidus slopes, as well as the partition coefficient, are summarized in Table 1, showing that this MD potential slightly overpredicts the liquidus slope and underpredicts the solidus slope, leading to an overpredicted partition coefficient k_E. The table also shows the pure aluminum melting point as determined by the kinetic coefficient evaluation, whose details are presented later. Again, the MD simulations slightly overpredict the melting point. Nevertheless, we believe that the phase diagram is sufficiently realistic for a meaningful analysis of Al–Cu alloy rapid solidification. We also verified that the solute diffusion coefficient in liquid phase is consistent with earlier work, as shown in the Supplementary material.

2.3. Free solidification simulation procedure

The initial system for non-equilibrium simulations contains coexisting solid and liquid phases and is prepared similarly to Yang et al. [22]. First, an FCC crystal of Al atoms is generated in a cuboid geometry, after which randomly selected Al atoms are replaced by Cu atoms such that composition of the solid and liquid regions is approximately equal to solidus and liquidus values corresponding to a given equilibration temperature, respectively. Then, atoms in the solid region are fixed, while the rest of the system is melted at relatively high temperature
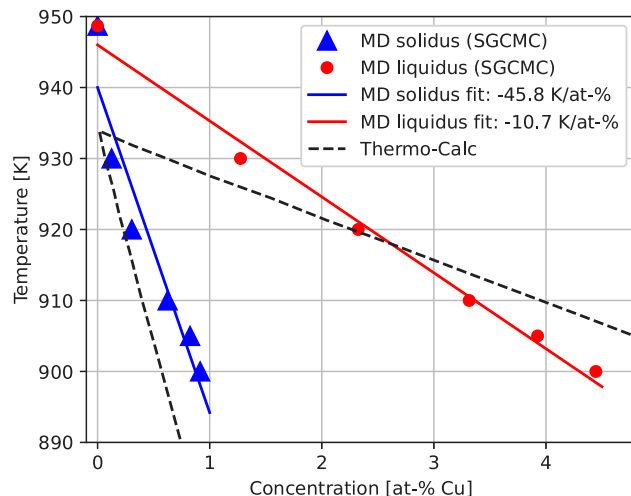

Fig. 1. Phase diagram computed from MD using semi-grand canonical Monte-Carlo (SGCMC) method (scatter points), with least-squares fitted solidus and liquidus lines (solid lines), compared to a phase diagram from Thermo-Calc TCAL6 database (dashed lines).

Table 1

Phase diagram characteristics. Pure aluminum melting points are estimated in the anisotropic kinetic coefficient analysis conducted for two interface orientations, (100) and (110). The liquidus and solidus slopes are estimated by assuming that the curves are linear near the Al-rich end of the phase diagram. Specifically, in the temperature ranging from the MD melting point T_m to a lower temperature $T = 900$ K. The equilibrium partition coefficient k_E is given by the ratio of the slopes.

Quantity	Experimental	MD	Unit
Al melting point (100)	933	948.7	K
Al melting point (110)	933	953.4	K
Liquidus slope m_L^{eq}	6.0	10.7	K/at%Cu
Solidus slope m_S^{eq}	57.9	45.8	K/at%Cu
Equilibrium k_E	0.103	0.233	

in an NP$_y$AT ensemble, where y is the solidification direction. In this ensemble, the total number of particles (N) and cross-sectional area (A) are kept constant, while the average temperature (T) and longitudinal pressure (P$_y$) are controlled by a Nosé–Hoover thermostat–barostat. Subsequently, the entire system is simulated in a NP$_y$AT ensemble in order to relax stresses. The relaxation temperature is defined by previously determined solidus and liquidus concentrations.

After this equilibration procedure, the solidification is started by setting the solute concentration in the liquid region to a chosen value and setting the thermostat temperature to the chosen quench, exemplified in Fig. 2. The quenching simulations are performed in a NP$_y$AT ensemble using a single global Nosé–Hoover thermostat. It should be noted that the latent heat release leads to local temperature rise above the thermostat target temperature, and the local solid–liquid temperature is monitored, as discussed further below in Section 2.5.

2.4. Solid–liquid interface position

The position of the solid–liquid interface is determined using a local order parameter, following Ref. [32]. The order parameter is evaluated by comparing the relative positions of the 12 nearest neighbors of a given atom to the ideal FCC configuration. In general, liquid, and solid regions display high and low order parameter values, respectively. The solid–liquid interface position is observed as a sudden change in the order parameter value, which can be captured by fitting a hyperbolic tangent function to the order parameter profile. The function fit is parametrized as $f(y) = a_0 + a_1 \tanh \frac{y-a_2}{a_3}$, where a_0, a_1 and a_3 are auxiliary fitting parameters, and the parameter a_2 represents the position of the interface in the direction of the propagation of the interface.
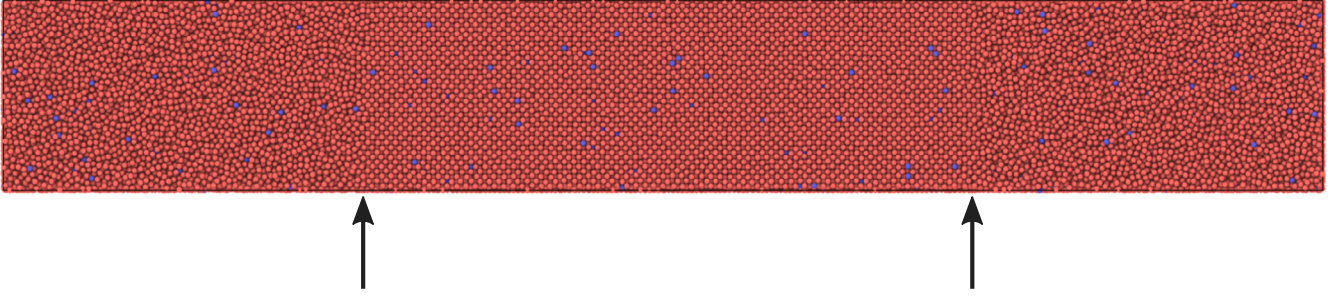
Fig. 2. Example system geometry. Aluminum and copper atoms are represented as red and blue spheres, respectively. The arrows indicate the current solid–liquid interfaces, which propagate horizontally.

Snapshots of the simulation are gathered at regular time intervals and the position of the interfaces is determined in each snapshot. The interfacial velocity is determined by the slope of a linear function fitted to the position data as a function of time.

2.5. Concentration and temperature profiles

Temperature profiles are obtained by averaging MD data over time, as described by Yang et al. [22]. A fine-grained profile is computed by subdividing the simulation cell into parallel bins along the direction of the solidification and counting the number of atoms in each bin $N(y)$. Correspondingly, the fine-grained solute profile is obtained by counting the number of solute atoms in each bin.

The fine-grained density profile for a given snapshot is thus given by

$$\rho_{\text{fine}}(y) = \frac{N(y)}{L_x L_z \delta_y}, \tag{1}$$

where L_x and L_z are the simulation cell dimensions in the respective directions, and δ_y represents the bin width in the longitudinal axis. In the solid region, the fine-grained profile displays regularly spaced peaks corresponding to crystal planes.

To compute the averaged density profile in the moving solid–liquid interface reference frame, the fine-grained profile of a given snapshot must be translated in the longitudinal direction.

The first snapshot in the simulation is defined as the reference frame and corrections in the longitudinal axis for subsequent snapshots are made relative to the reference. The position of the crystal plane closest to the interface is determined for each snapshot using a peak detection algorithm. Thus, the correction for a given snapshot is equal to the difference in y-coordinate between this position and the position in the reference. A Savitzky–Golay smoothing filter [33] is applied to the fine-grained profile of a given snapshot to improve the accuracy of the peak detection algorithm. Finally, the average of these corrected fine-grained profiles is computed.

To smooth out the oscillating effects due to crystal planes, coarse-grained net density $\rho(y)$ and solute density profiles $\rho_{\text{Cu}}(y)$ are computed by applying a finite-impulse-response (FIR) smoothing filter [22] to the corresponding averaged fine-grained density profiles. Lastly, the coarse-grained solute concentration profile is given by the following ratio:

$$c(y) = \frac{\rho_{\text{Cu}}(y)}{\rho(y)}. \tag{2}$$

Temperature profile $T(y)$ is calculated using the coarse-grained kinetic energy profile $K(y)$, by applying a FIR filter on the fine-grained kinetic energy profile, which is given by

$$K_{\text{fine}}(y) = \frac{1}{2L_x L_z \delta_y} \left(\sum_{i=1}^{N(y)} m_i v_i^2 \right), \tag{3}$$

where L_x and L_z refer to the simulation cell dimensions in the respective Cartesian directions perpendicular to the solidification direction y,

δ_y represents the bin width, m_i is the mass and v_i the velocity magnitude of atom i. The coarse-grained temperature profile is thus given by

$$T(y) = \frac{K(y)}{3/2 k_B \rho(y)}, \tag{4}$$

where k_B is Boltzmann's constant.

2.6. Non-equilibrium partition coefficient

The non-equilibrium partition coefficient is evaluated as a ratio between the solid and liquid phase solute concentrations, which are estimated from MD data as follows. A time interval is chosen during which a given interface progresses in the solidification direction from y_{start} to y_{end}. These interface positions are obtained with the procedure described in Section 2.4. The liquid phase solute concentration c_L is estimated from the snapshot corresponding to the start of the considered time interval, and the solid phase solute concentration c_S is estimated from the snapshot corresponding to the end of the time interval. In both cases, the concentration estimation accounts for all atoms located in the region delimited by y_{start} and y_{end} in the corresponding snapshot. The instantaneous partition coefficient is thus obtained as the ratio $k = c_S/c_L$. This procedure is repeated by shifting the start of the time interval to the following snapshot until the edge time interval reaches the last snapshot. The time-averaged non-equilibrium partition coefficient is given by the arithmetic average of instantaneous partition coefficient values, while the error of the measurement is estimated as the standard deviation of the instantaneous partition coefficients relative to the mean. Cases that reached complete solute trapping regime were verified to have negligible solute partitioning by visually inspecting the solute distribution bins $c(y)$, and the evaluated partition coefficient $k = c_S/c_L$ fluctuates close to value 1.0, within error bars, as shown later in Section 3.1.3.

We chose to evaluate partition coefficient k as a time-average of the instantaneous partition coefficients, as an alternative to the method discussed by Yang et al. [22], where solid-side and liquid-side solute concentrations (c_S and c_L) are estimated from the time-averaged solute concentration profile relative to the moving solid–liquid interface. In our experience, the partition coefficient values obtained using this latter method consistently saturated to a value of approximately $k = 0.9$ in the complete solute trapping regime, instead of $k \approx 1$.

We will compare the MD-derived partition coefficient (k vs. V data) to the partition coefficient according to the continuous growth model (CGM) [34]:

$$k(V) = \frac{k_E + V/V_D}{1 + V/V_D}, \tag{5}$$

where V_D is the interface diffusive speed according to the CGM. In addition, the MD-derived k vs. V data is compared to local non-equilibrium model (LNM) of solute transport [35]:

$$k^{LNM}(V) = \begin{cases} \frac{k_E(1 - V^2/V_{\text{Db}}^2) + V/V_{\text{Di}}}{(1 - V^2/V_{\text{Db}}^2) + V/V_{\text{Di}}}, & V < V_{\text{Db}} \\ 1, & V > V_{\text{Db}}, \end{cases} \tag{6}$$

where V_{Di} represents the interface diffusive speed, and V_{Db} represents the bulk liquid diffusive speed. Note that we do not assign direct physical meaning to parameters V_D, V_{Di}, and V_{Db}, but rather treat them as free parameters fitted to the MD data.

2.7. Solid–liquid interface temperature

Due to latent heat release, the true system temperature increases above the target quench temperature set to the thermostat [21]. Moreover, classical MD only accounts for heat transport due to phonons (atomic vibrations), while in metals, heat is transported mostly via electrons, whose motion are not explicitly considered in bond-order potential based molecular dynamics. While the electronic heat transport can be accounted for with, e.g., the two-temperature molecular dynamics approach [36], we do not consider them in this work for simplicity. Moreover, as we use a single thermostat, the temperature is expected to increase around the solid–liquid interface.

Therefore, temperature around the solid–liquid interface is measured. Two different methods were employed to estimate the temperature at the interface, depending on the system size. For smaller systems ($N_{\mathrm{p}} = 56\,000$), the temperature profile displayed relatively large fluctuations, for which, therefore, the interface temperature T is derived from the corresponding coarse profile by evaluating the average temperature in the range $y \in [-5, 5]$ Å in the reference frame with the origin coinciding with the propagating solid–liquid interface. For larger systems ($N_{\mathrm{p}} > 200\,000$), fluctuations in the temperature profile are less significant, and the temperature clearly reaches a maximum value approximately at $y = 0$, i.e., at the center of the interface. For all system sizes, statistical error is related to the standard deviation of the temperature values in this range, which corresponds to the solid–liquid interfacial region. In these simulations, T_{MD} corresponds to the maximum value after an additional Savitzky–Golay smoothing filter has been applied to the coarse profile, to further reduce the fluctuations.

The temperature (T) vs. velocity (V) data from MD is compared to the following analytical model for the interface temperature [37]:

$$T = T_m - f(\alpha, k(V))m_L^{eq}c_L - \Gamma\kappa - \frac{V}{\mu_k},\tag{7}$$

where T_m is the pure material melting point, m_L^{eq} is the equilibrium liquidus slope, c_L is the solute concentration at the interface, Γ is the Gibbs–Thompson coefficient for the interface curvature correction, κ is the curvature, μ_k is the linear kinetic coefficient and

$$f(\alpha, k(V)) = \frac{1 - k(V) + [k(V) + \alpha \cdot (1 - k(V))]\ln(k(V)/k_{\mathrm{E}})}{1 - k_{\mathrm{E}}}\tag{8}$$

is the velocity-dependent undercooling correction, where α is a parameter that can be used to tune the extent of solute drag. A parameter value $\alpha = 0$ corresponds to no solute drag, and $\alpha = 1$ to full solute drag. We neglect all curvature effects in our analyses, i.e., we set $\kappa \approx 0$.

2.8. Solid–liquid interface energy and its anisotropy

To compute solid–liquid interface free energy γ and its anisotropy, we used the capillary fluctuation method (CFM) [32]. In this technique, the interfacial stiffness, $\gamma + \gamma''$, is computed, where $\gamma'' = d^2\gamma/d\theta^2$, where θ is the angle between the normal to the interface and the solidification direction (y axis). The solid–liquid interface position Fourier amplitude averages are derived from MD equilibrium simulations and used to obtain the stiffness components. The stiffness components are used to evaluated γ by using an expansion of the free energy γ with respect to the interface normal vector $\hat{n}$ [38].

To sample sufficiently large wavelengths, the method requires simulating a system with relatively large cross-sectional area. In this work we consider both (100) and (110)-oriented solid–liquid interfaces. The equilibrium simulations were performed at two target thermostat-set quench temperatures: at $T_1 = 940$ K and $T_2 = 900$ K. The temperature T_1 corresponds approximately to the melting point of pure aluminum

predicted by the interatomic potential. At T_2, the liquidus and solidus solute concentrations predicted by the potential are given by $c_L = 4.45\,\mathrm{at.\%Cu}$ and $c_L = 0.915\,\mathrm{at.\%Cu}$.

The simulation system is first melted at a relatively high temperature in the NPT ensemble. Following this, the system is relaxed in the NPT ensemble at the given temperature (T_1 or T_2). Initial system configurations used for generating CFM data are created by performing a mixed MD–MC simulation from which the configurations are extracted at fixed time intervals. The simulation runs for sampling fluctuation amplitudes were performed in a microcanonical NVE ensemble. These samples were employed in the calculation of the averaged Fourier amplitudes. The height profile of the solid–liquid interface is determined from data, and the resulting averaged Fourier amplitudes are computed. Finally, interfacial free energies and their anisotropies are derived from relations given in the Supplementary material.

3. Results and discussion

In what follows, we first present the evaluation of solid–liquid interface properties relevant to rapid solidification (Section 3.1.2), after which the rapid solidification structures are analyzed with respect to point defects, chemical ordering, and solid phase content (Section 3.2).

3.1. Solid–liquid interface properties

3.1.1. Anisotropic solid–liquid interface energy
The solid–liquid interface energies, measured with capillary fluctuation method (CFM), are shown in Table 2 at 940 K for pure aluminum as well as at 900 K for Al–Cu alloy set to its equilibrium solidus (0.915 at.%Cu) and liquidus (4.45 at.%Cu) concentrations, together with earlier MD simulations and experiments from literature. The Al–Cu interface energy is within the error bars of the experiments, and slightly below the earlier MD simulations.

In our simulations, the solid–liquid interface energy magnitude (γ_0) increases with addition of copper (while the melting point decreases from the pure aluminum to the dilute Al–Cu alloy).

It is known that in elemental metals solid–liquid interface energy decreases with decreasing temperature [39]. In studies performed on binary Cu–Zr [40] and Al–Sm [41] systems, the interface energy magnitude γ_0 increased with decreasing temperature. Wang et al. [41] note that in both cases Al–Sm and Cu–Zr show a very small solid solubility and a relatively large atomic size mismatch. In contrast, Al and Cu show a relatively small size mismatch and large solubility.

To systematically evaluate the temperature–concentration dependence of a binary alloy solid–liquid interface energy, the semi-grand canonical MC based technique by Frolov and Mishin can be used [42]. However, this was out of the scope for the current study.

3.1.2. Free solidification simulations
Free solidification simulations were carried out to determine kinetic properties of the solid–liquid interface: mobility or kinetic coefficient, as well as solute trapping kinetics in terms of $k - V$ data and the solute drag effect. The point defects, chemical ordering, and crystalline phases of these simulated rapid solidification structures are then analyzed.

Rapid solidification simulations were performed using various nominal alloying levels c_{nom} and nominal thermostat-based quench temperatures T_{nom}, and the corresponding average velocities V_{av} and the average solid–liquid interface temperature T_{MD} for Al–Cu alloy and pure aluminum cases oriented either to (100) or (110), as indicated. These are listed in Table 3. Examples of solidification velocity fitting, as well as the final resulting velocity for each simulation case, are shown in the Supplementary material. Table 3 also shows the magnitude of the solidification driving force is quantified as the dimensionless supersaturation Ω for Al–Cu alloys, and as dimensionless undercooling Δ for the pure aluminum. We use the following definitions: $\Delta = \frac{T_m - T_{MD}}{L/C_p}$, where L is the latent heat of fusion, and C_p is the heat capacity; $\Omega =$

Table 2
Solid–liquid parameters extracted from MD simulations.

	γ_0 (mJ/m^2)	ϵ_1 (%)	ϵ_2 (%)
BOP-MD^a (Al–Cu at $T = 900$ K)	127 ± 3	5.3 ± 0.6	0.14 ± 0.12
BOP-MD^a (pure Al., $T = 940$ K)	104 ± 3	3.8 ± 0.7	0.1 ± 0.2
MEAM-MD^b	172.6	5.7	−0.37
EAM-MD^c	120 ± 6	1.4 ± 0.4	–
EAM-MD^d	149.0	–	–
Exp.^{e}	$158 \pm 30 - 168.9 \pm 21$	–	–
Exp.^{f} (Al–4.0 wt% Cu)	–	0.97	–

^{a} Present work, ^{b} Ref. [43], ^{c} Ref. [44], ^{d} Ref. [45], ^{e} Refs. [46–48], ^{f} Ref. [49]

	Equilibrium k_E	V_D (m/s)	V_{Di} (m/s)	V_{Db} (m/s)
BOP-MD^a	0.233	2.3 ± 0.3	2.9 ± 0.3	13 ± 1
Exp.^{b}	0.15	6.7	–	–
Exp.^{c}	0.10	–	–	–

^{a} Present work, ^{b} Ref. [50], ^{c} Thermo-Calc software TCAL6 database

	β_0 (s/m)	β_{100} (s/m)	μ_{100} (m/s/K)	μ_{110} (m/s/K)	$\epsilon_k = (\mu_{100} - \mu_{110})/(\mu_{100} + \mu_{110})$
BOP-MD (pure Al.)^a	–	–	1.03 ± 0.04	0.85 ± 0.03	0.0943
BOP-MD (1 at.%Cu)^a	0.121	0.110 ± 0.018	1.11	–	–
BOP-MD (2 at.%Cu)^a	0.0839	0.076 ± 0.005	0.80	–	–
EAM-MD^b	–	–	1.573	1.283	0.102
β_{ana} (1 at.%Cu)	0.0272	–	–	–	–
β_{ana} (2 at.%Cu)	0.0136	–	–	–	–

^{a} Present work, ^{b} Ref. [51], ^{c} Ref. [34]

Table 3
Solidification parameters and velocities for each MD simulation case considered. T_{nom} gives the nominal (thermostat) quench temperature, c_{nom} gives the nominal solute concentration, Ω is the dimensionless supersaturation, N_p is the number of atoms, V_{av} is the average solidification velocity of both propagating interfaces, T_{MD} is the average temperature in the MD simulations, and Δ is the dimensionless undercooling. Table (a) shows data for dilute Al–Cu alloy simulation with (100)-oriented interfaces, while table (b) shows data for pure Al simulations (column 'ori' gives the orientation of the interface).

(a)

ori	T_{nom} (K)	c_{nom} (at%Cu)	Ω	N_p	V_{av} (m/s)	T_{MD} (K)
(100)	880	4	0.50	56 000	0.30	880.7
(100)	900	2.5	0.52	56 000	0.39	901.5
(100)	900	2	0.68	56 000	1.72	901.2
(100)	900	1.5	0.77	56 000	2.01	905.0
(100)	900	1.5	0.77	224 000	3.84	905.0
(100)	880	2	0.82	56 000	8.99	888.3
(100)	880	2	0.82	224 000	10.44	888.7
(100)	860	2	0.91	56 000	20.96	875.6
(100)	880	1	0.98	224 000	25.32	898.8
(100)	880	1	0.99	56 000	26.62	898.6
(100)	860	1	1.05	56 000	39.77	886.2

(b)

ori	T_{nom} (K)	c_{nom} (at%Cu)	Δ	N_p	V_{av} (m/s)	T_{MD} (K)
(110)	910	0	0.043	217 740	18.9	925.7
(100)	910	0	0.038	224 000	22.8	927.3
(110)	900	0	0.058	217 740	24.1	920.8
(100)	900	0	0.057	224 000	29.9	921.2
(110)	880	0	0.099	217 740	35.5	907.1
(100)	880	0	0.097	224 000	43.2	907.8
(110)	860	0	0.149	217 740	44.5	890.4
(100)	860	0	0.127	224 000	54.9	897.6

$-\frac{c_l^{eq} - c_{nom}}{(1 - k_E)c_l^{eq}}$ is the dimensionless supersaturation ($c_l^{eq} = \frac{T_m - T_{MD}}{m_l^{eq}}$). It can be seen that the MD simulations self-consistently produces solidification velocities that increases monotonically with the driving force (Ω or Δ), when it is noted that the (110) oriented interfaces propagate slower due to the reduced interface mobility.
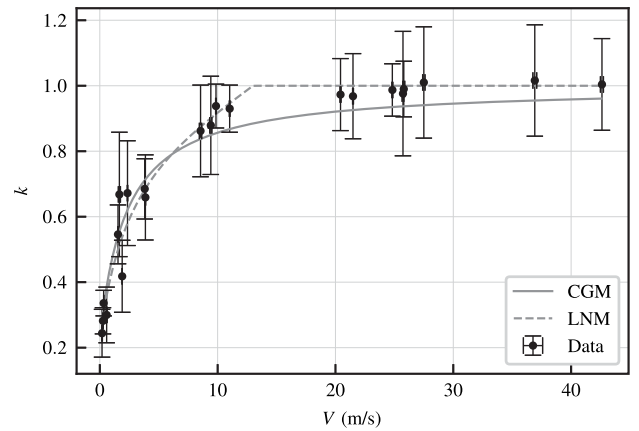

Fig. 3. Non-equilibrium partition coefficient k vs. interfacial velocity V. Round markers correspond to MD simulation data, the continuous line represents the least-squares fit of the continuous growth model relation with respect to the parameter V_D. Similarly, the dashed line corresponds to the least-squares fit of the local non-equilibrium model relation with respect to the parameters V_{Di} and V_{Db}. The MD data is based on all Al–Cu results carried out, specified in Table 3a.

3.1.3. Partition coefficient versus interfacial velocity

The results of the partition coefficient estimation are given in Fig. 3, showing the expected trend of increasing k with V, and a saturation at high velocities. The Supplementary material shows additional data related to the determination of the partition coefficient. The fitted parameter for the CGM is $V_D = 2.3 \pm 0.3$ m/s, and the fitted parameters for the LNM are $V_{Di} = 2.9 \pm 0.3$ m/s and $V_{Db} = 13 \pm 1$ m/s. Fig. 3 contains error bars for each data point, showing that the interface velocity has negligible error bars, whereas the partition coefficient data has relatively large error bars, which decreases with the system size and nominal copper content, as expected. These velocities are consistent with earlier simulations, as shown in Table 2.

3.1.4. Solute drag analysis

Another key feature of solute trapping kinetics is the solute drag effect. We evaluated the solute drag parameter following Kavousi et al. [24]. The idea is to fit a line to the (V, ΔG_{eff}) data as a function

of drag coefficient (α), and see which drag coefficient gives the best fit to (V, ΔG_{eff}), i.e. gives the largest coefficient of determination (R^2) for a linear fit to the $k - V$ data.

The effective solidification driving force ΔG_{eff} is given as follows [24]:

$$\Delta G_{\text{eff}} = \Delta G_{DF} - \alpha \Delta G_D, \tag{9}$$

where the chemical free energy change in solidification is represented by ΔG_{DF}, which is given by the following expression [24]:

$$\Delta G_{DF} = c_S \Delta \mu_B - (1 - c_S) \Delta \mu_A, \tag{10}$$

where $\Delta \mu_A$ and $\Delta \mu_B$ are the differences of chemical potential between solid and liquid phases of the solvent (A) and solute (B), respectively, and c_S is the solid-side solute concentration.

ΔG_D represents the free energy portion of the energy dissipated due to solute drag, given by [24]:

$$\Delta G_D = (c_L - c_S)(\Delta \mu_A - \Delta \mu_B), \tag{11}$$

and α is the solute drag coefficient. The effective driving force involves obtaining quantities related to chemical potential differences for solvent and solute atomic species in both solid and liquid phases, $\Delta \mu_S$ and $\Delta \mu_L$, respectively. These values were obtained using semi-grand canonical ensemble simulations. The temperature- and concentration-dependent free energy in solid and liquid phases, $G_S(T, c)$ and $G_L(T, c)$, respectively, were calculated as well. $\Delta \mu_A$ and $\Delta \mu_B$ are related to these quantities as follows [24]:

$$\Delta \mu_A = G_S(T, c_S) - G_L(T, c_L) - c_S \Delta \mu_S + c_L \Delta \mu_L \tag{12}$$

$$\Delta \mu_B = G_S(T, c_S) - G_L(T, c_L) + (1 - c_S)\Delta \mu_S - (1 - c_L)\Delta \mu_L \tag{13}$$

Interpolation was employed to obtain free energy and chemical potential difference values corresponding to interfacial temperature T_{MD} and concentrations c_S and c_L data extracted from the free solidification simulations. The chemical potential values, used as a basis for the interpolation, are shown in the Supplementary material.

Fig. 4 shows the (V, ΔG_{eff}) data without solute drag ($\alpha = 0$), full solute drag ($\alpha = 1$), and the optimal solute drag coefficient ($\alpha = 0.38$) with the largest R^2 value. The optimized solute drag coefficient value is consistent with earlier [22,24], where a partial drag coefficient was found.

3.1.5. Anisotropic kinetic coefficient

The anisotropic kinetic coefficient is determined by direct measurement of the solid–liquid interface velocity versus interfacial temperature for (100) and (110) directions for pure aluminum. Fig. 5 shows the resulting MD data. We performed a linear least-squares fit to the data with $T > 900$ K, for which the scatter data are tightly following a linear line, while in particular for the 110 data around 890 K, the scatter points start to show deviation from the linearity. Ruling out the $T > 900$ K data lead to consistent estimates of the melting point (following the fitted lines to $V = 0$ m/s).

The resulting anisotropic kinetic coefficients for orientations (100) and (110) are given in Table 2. These values are consistent with the DFT-based model of Mikheev and Chernov and the Broughton–Gilmer–Jackson theory based on the LJ system, which both predict a ratio $\mu_{100}/\mu_{110} = 1.41$ [45], whereas our simulations give a value $\mu_{100}/\mu_{110} \approx 1.21$. Earlier studies on MD simulations of FCC metals such as Tb [52], Ni [53] and Au [54] have produced similar results. By extrapolating the interface temperature to zero velocities, for both (100) and (110) data in Fig. 5, the pure aluminum melting point can be estimated to be $T_m = 948.9$ K (100) and $T_m = 948.2$ K (110), respectively. These melting point estimates are within the range reported by the bond-order potential developers [29]: $T_m \approx 947 K \pm 36$ K.

In addition to the pure aluminum based kinetic coefficient, we evaluated the kinetic coefficient for Al–Cu alloys according to Kavousi et al. [24], which requires knowledge of the solute drag coefficient
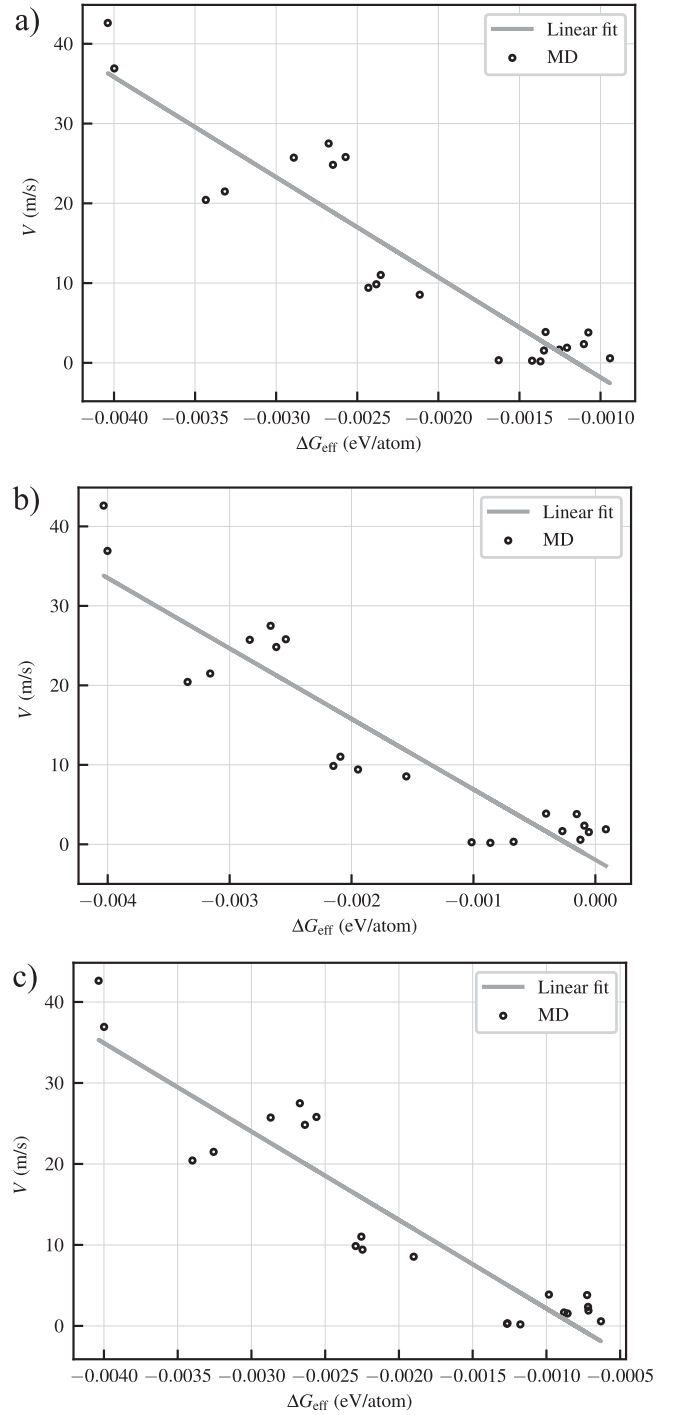
Fig. 4. Results of the solute drag coefficient α analysis using the Al–Cu solidification cases specified in Table 3a. Plots show the interfacial velocity V versus the effective solidification driving force ΔG_{eff} with different levels of solute drag. Circles indicate MD data and solid lines correspond to the linear least-squares fit. In graph (a) the solute drag coefficient is $\alpha = 0$, in graph (b) $\alpha = 1$ and in graph (c) $\alpha = 0.38$, which corresponds to the optimal linear fit, as measured by the R^2 value.

α, concentrations in the liquid phase of the system c_{nom} and c_L, interfacial velocity V, interfacial temperature T, and equilibrium and non-equilibrium partition coefficients k_E and $k(V)$. The following expression is plotted versus V [24]:

$$\beta = \frac{1 + \frac{T_L - T}{m_L^{eq} c_{\text{nom}}} - \frac{c_L}{c_{\text{nom}}} f(\alpha, k)}{1 - k_E}, \tag{14}$$
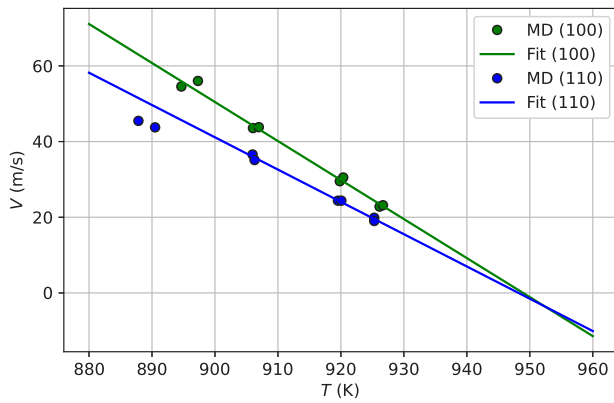
Fig. 5. Solid–liquid interface velocity with respect to interfacial temperature for pure aluminum, using simulation cases from Table 3b. Colored marks indicate data points obtained from MD simulations, and solid lines show the corresponding linear least-squares fit. Green and blue circles indicate (100) and (110)-oriented interfaces, respectively. The pure aluminum melting point estimations given by the *x*-axis intercept of the corresponding linear fits are $T_m = 948.9$ K and $T_m = 948.2$ K for the (100) and (110) interface orientations, respectively.

where m_L^{eq} is the liquidus slope, $T_L = m_L^{eq} c_{\text{nom}}$ is the estimated liquidus temperature, and $f(\alpha, k)$ velocity-dependent undercooling correction given previously. Plots are shown in Fig. 6 for two separate solute concentrations ($c_{\text{nom}} = 1.0$ at%Cu and $c_{\text{nom}} = 2.0$ at%Cu) resulting in the following kinetic coefficient values: $\beta_1 = 0.110$ s/m and $\beta_2 = 0.076$ s/m, respectively. Alternatively, the kinetic coefficient can be expressed as $\mu_k = 1/(\beta c_{\text{nom}} m_L^{eq}(1 - k_E))$, resulting in $\mu_{k,1} = 1.11$ m/s/K and $\mu_{k,2} = 0.80$ m/s/K. These values are consistent with our earlier results.

We also computed an analytical estimate of the kinetic coefficient [24,34]:

$$\beta_{ana} = \frac{1}{V_s(1 - k_E)^2 c_{nom}}, \tag{15}$$

where V_s is the speed of sound of the metal melt, for which we used a value for pure aluminum from Ref. [55], $V_s \approx 4561$ m/s. We used an experimental equilibrium partition coefficient $k_e \approx 0.103$. As shown in Table 2, compared to MD derived values, the resulting analytical kinetic coefficients are significantly smaller: ~22% of the MD value for 1 at.%Cu, and ~16% of the MD value for 2 at.%Cu.

3.1.6. Temperature vs. velocity in continuous growth model and MD

After calibrating the solute trapping kinetics and kinetic coefficient, we verify that MD self-consistently reproduces the temperature–velocity behavior of the continuous growth model (Eq. (7)).

For evaluating the continuous growth model temperature using Eq. (7), several parameters were employed. The pure aluminum melting point was extrapolated to zero velocity from the kinetic coefficient analysis of Fig. 5, the liquidus slope was determined using equilibrium MD simulations, the curvature κ was set to zero, the liquid-side solute concentration (c_L in Eq. (7)) was determined in connection with the partition coefficient evaluation (Section 3.1.3), and the linear kinetic coefficient μ_k was determined as described in Section 3.1.5.

Fig. 7 shows comparisons between model (Eq. (7)) and free solidification MD simulations. The model error bars originate from errors in the following quantities extracted from MD simulations: melting point T_m, interfacial velocity V, kinetic coefficient μ_k, liquidus slope m_L^{eq}, solute drag coefficient α, equilibrium k_E, diffusive velocity V_D, and liquid-side solute concentration c_L. The T vs. V data from MD is in good overall agreement with the continuous growth model, although the MD data seems to systematically underpredict the theoretical prediction to some extent. This underprediction can be related to the evaluation of the solid–liquid interface temperature, which is a somewhat complicated procedure prone to errors. This error can be alleviated by increasing the system area (normal to the solidification direction), or by using a large number of thermostats.
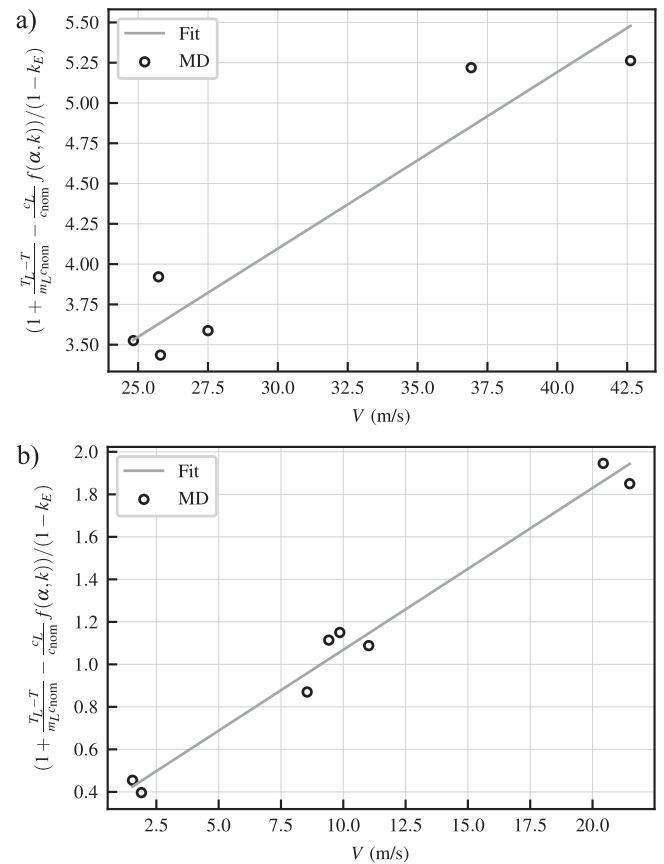

Fig. 6. Kinetic coefficient β according to Eq. (14) versus interfacial velocity. Circles represent MD data and lines show the corresponding linear least-squares fit. Graph (a) shows data for average liquid-side solute concentration $c_{\text{nom}} = 1.0$ at%Cu and graph (b) shows data for $c_{\text{nom}} = 2.0$ at%Cu from Table 3a.

3.2. Crystal defects, chemical ordering, and phase analysis

Aluminum alloys are known to exhibit chemical ordering, i.e. deviation from ideal random solid solution in the α (FCC) aluminum phase. For heat-treatable alloys, such as the 2XXX series aluminum–copper alloys, this chemical ordering, or clustering, is the first step in the sequence leading to precipitation, which is an important strengthening mechanism for these alloys [6,17,18]. Also, it is interesting to analyze the relationship between point defects and chemical ordering. Vacancies seem to be particularly important for pre-precipitation, by acting as nucleation sites of Guinier–Preston zones [3], compared to larger scale defects such as dislocations.

3.2.1. Point defect content

Rapid solidification structures were investigated for vacancies using the Wigner–Seitz defect analysis method implemented in OVITO [56]. To perform the analysis, an energy minimization procedure was conducted using LAMMPS on the snapshot of the fully solidified system, where in essence, the system temperature is dropped to 0 K. As a result, an atomic configuration is obtained free of entropic deviation caused by thermal motion [13]. Then, defects (interstitials or vacancies) are easily identified in the Wigner–Seitz defect analysis. In the analysis, the energy-minimized configuration is compared to a template lattice representing an ideal FCC crystal free of defects, thereby allowing for an explicit identification of point defects. An example of a vacancy and a nearby interstitial is shown in Fig. 8; as discussed more closely below, the vacancies and interstitials often form as a Frenkel defect pair in these MD simulations.
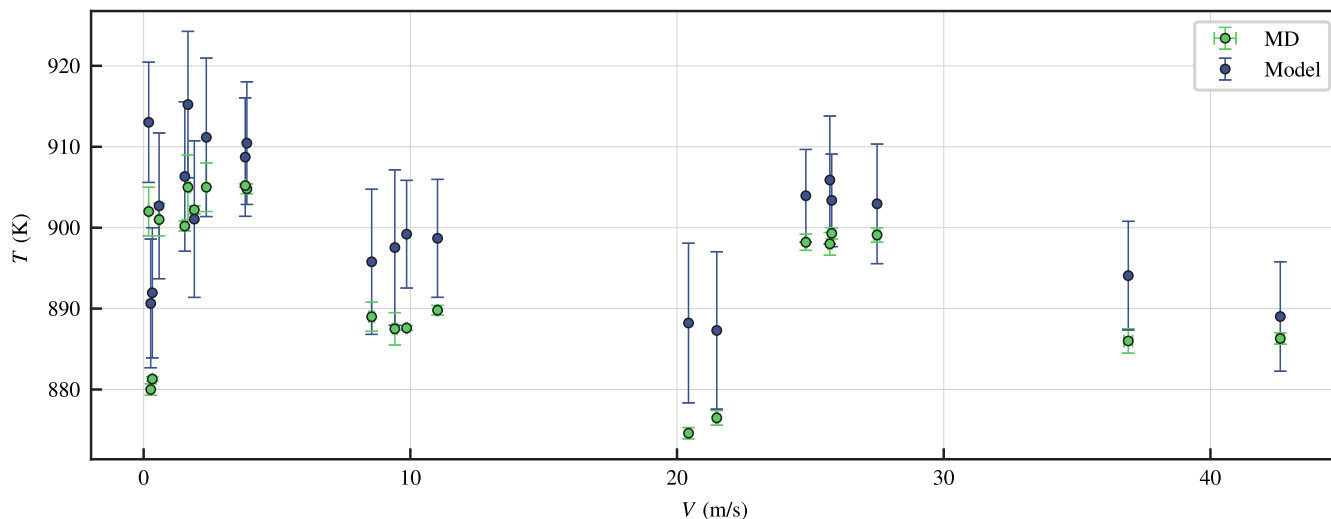
Fig. 7. Green markers indicate interfacial temperatures derived from Al–Cu MD simulations in Table 3a, while blue markers indicate the model prediction for interfacial temperature at the same velocity values. Error bars for the model predictions originate from errors associated with quantities extracted from MD simulations.
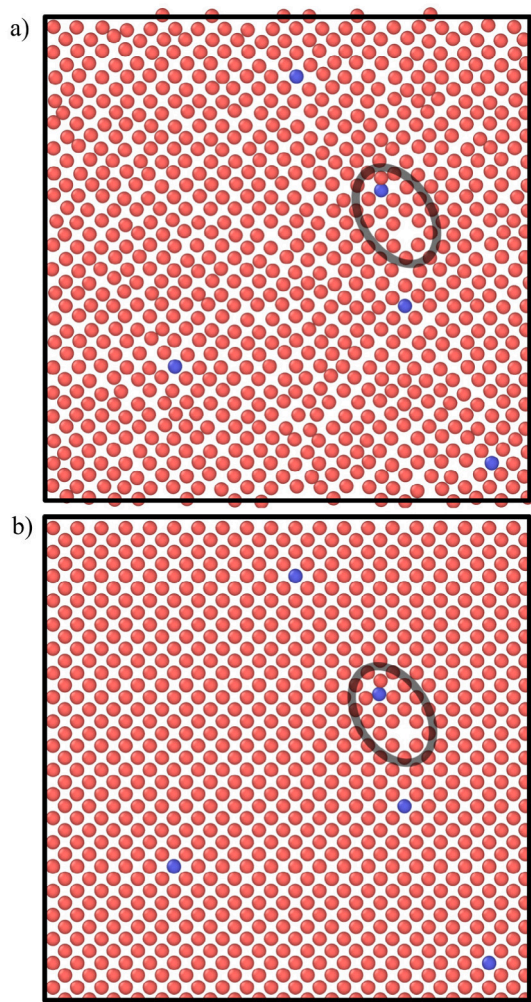

Fig. 8. Isolated crystal planes displaying a Frenkel vacancy–interstitial pair. The ovals indicate the location of a vacancy and an interstitial copper atom. Picture (a) shows the given crystal plane before the energy minimization procedure, and picture (b) shows the corresponding crystal plane after the procedure. Simulation parameters: $T_{nom} = 880$ K and $c_{nom} = 1$ at%Cu, resulting in an average interfacial velocity of $V_{av} = 25.32$ m/s.

The defect concentrations for several simulations are shown in Fig. 9, as a function of the interfacial velocity. The first evident feature of these simulations is that at higher velocities, the interstitial and vacancy concentrations are equal. We argue that this equality is due to the fact that at diffusionless solidification of single crystals, point defects are exclusive generated as interstitial–vacancy pairs (Frenkel defects). This point defect formation is analogical to results of Nordlund and Averback [57], where they reported Frenkel pair generation in a superheated FCC Cu system, as well as tests for FCC Au.

More specifically, the Frenkel defect pairs seem to form as follows. As the diffusionless solidification velocity regime is approached (slightly below 10 m/s), the solid–liquid front propagates too fast for atoms to diffusively react to (or hop around) the solid–liquid interface. Therefore, the solid–liquid interface is unable to act as a proper source or sink for point defect formation. Furthermore, as we use periodic boundary conditions, the boundaries are unable to produce point defects [57]. It should be noted that in identifying the defects, we neglect the solidification direction (y-direction) boundary region when the two solidification fronts meet and start to interact. Therefore, as there are no sources or sinks for point defect generation, any point defects need to form as interstitial–vacancy pairs, i.e. as Frenkel defects [57].

Below complete solute trapping regime, at solidification velocities below roughly 10 m/s, we believe that the solid–liquid interface is able to act as a source for point defects, allowing for an independent formation of interstitials and vacancies; this can potentially also explain the fact that the point defect content does not simply decrease monotonously with the velocity. It should be noted that some of the Frenkel defect pairs might become unstable as the solid is cooled to ambient temperatures, if the interstitial–vacancy pair distance is sufficiently small for recombination to occur [57].

Another notable feature in Fig. 9 is that, overall, a significant number of interstitial defects are observed. The presence of interstitial defects in rapid solidification is consistent with MD simulations of Ashkenazy and Averback [58], who suggest that solidification proceeds, in cubic crystals, through annihilation of interstitials around the solid–liquid interface; typically, interstitials have a relatively high mobility and are thus quickly annihilated after they form, whereas at large quenches (rapid solidification conditions), the thermally activated interstitial mobility decreases exponentially and get trapped more readily. These results are consistent with experiments by Refs. [59,60], who found high interstitial concentrations in single crystal aluminum near its melting point. This is in contrast to an earlier embedded atom method (EAM) based analysis where no interstitials were found for pure
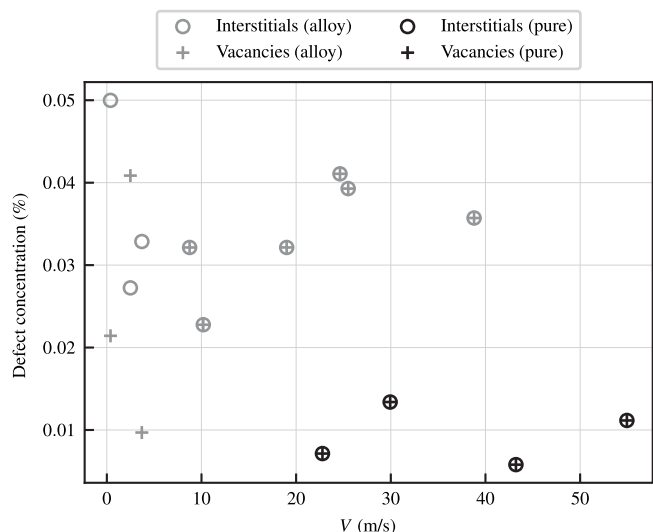
Fig. 9. Defect concentrations versus average interfacial velocity. Circles and crosses indicate interstitial and vacancy atoms, respectively. Gray markers indicate defect data for Al–Cu (Table 3a), while black markers indicate pure aluminum data (Table 3b).

aluminum [13], while our simulations do lead to vacancy concentrations in similar levels at the considered velocities (below 20 m/s) to those found in Ref. [13]. The high interstitial concentration is explained by this bond-order potential being parametrized to produce a relatively low interstitial formation energy, only slightly higher than the vacancy formation energy [29]; this is consistent with ab-initio simulations carried out in Ref. [61]. It should be noted, however, that another ab-initio computation predicted a significantly higher interstitial energies [62]. Finally, the high interstitial concentrations in our simulations are in agreement with work by Nordlund and Averback [57], who found relatively high interstitial concentrations in equilibrium near the melting point for FCC Cu, and even higher in pulse-heated conditions which represent non-equilibrium conditions; our rapid solidification simulations are at an analogical non-equilibrium condition.

Considering the effect of copper alloying in Fig. 9, it seems that solute atoms increase the production of defects, as the concentration of these are consistently 3 or 4 times larger in alloys than in pure aluminum, even at similar interfacial velocities. If we consider the binary alloys and the pure metal separately, there are no evident trends with respect to the interfacial velocity, since in both cases the defect concentrations stay approximately constant on the plotted velocity range. This is consistent with earlier work by Zhang and co-workers [13] for pure aluminum, where vacancy content starts to increase significantly only at higher solidification velocities, in the range of 30–50 m/s, which are not considered in our simulations. Similarly, the theoretical work of Hillert [63] suggests that a relatively high solidification velocity (e.g., orders of magnitude above 1 m/s) are required to achieve notable vacancy trapping, i.e. an increase in vacancy concentration above its equilibrium values.

Point defects do form even in thermodynamic equilibrium due to entropic effects, but their amount is increased in rapid solidification of metals due to the partial freezing in of the liquid – i.e. imperfect reorganization of the disordered liquid – into an ordered lattice [12, 13,63].

3.2.2. Chemical ordering

The chemical ordering, i.e. copper distribution relative to vacancies and to other copper atoms, was determined as the nearest neighbor distribution in Fig. 10. The graphs show the frequency of solute atoms in the 12 nearest lattice sites neighboring vacancies (Fig. 10a) and copper atoms (Fig. 10b) for a single simulation case. This distribution is
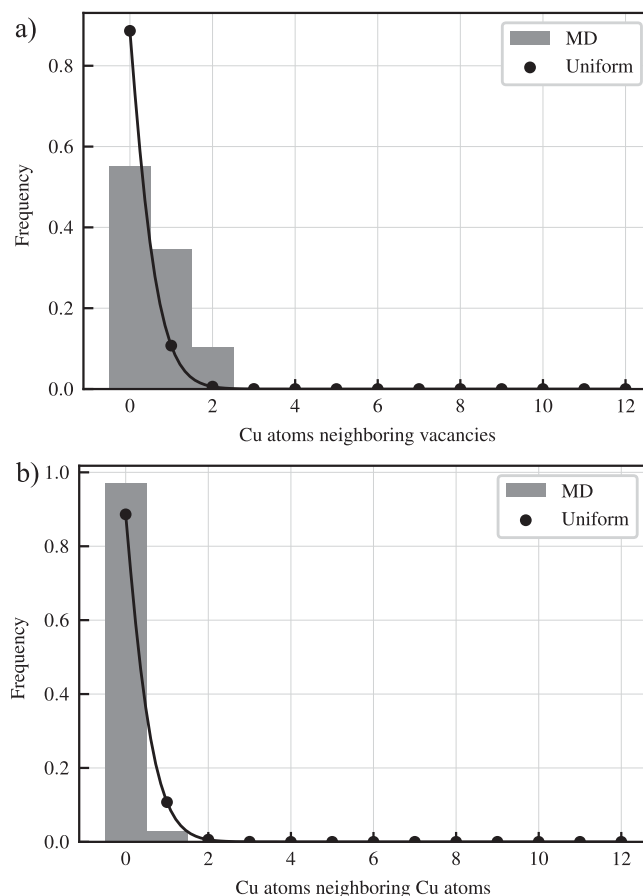

Fig. 10. Frequency of copper atoms in the 12 nearest atoms relative to (a) vacancies, and (b) copper atoms, where the black dot-curves show the theoretical uniform random distribution, and the gray bars show the MD results. The structure is fully solidified with parameters $T_{nom} = 880$ K and $c_{nom} = 1$ at%Cu, resulting in an average interfacial velocity of $V_{av} = 25.32$ m/s.

compared to the ideal random distribution of solute atoms (black solid lines).

In Fig. 10a, it can be seen that the copper atoms are more likely to be near vacancies, instead of being uniformly distributed in the structure. In other words, vacancies seem to attract copper atoms. This is consistent with Ref. [17], where it was pointed out that in aluminum, solute–vacancy interaction is not mediated by simple elastic strains, which would lead to vacancy–copper repulsion.

In contrast, Fig. 10b shows that copper atoms are less likely to be found next to each other; in other words, copper atoms seem to repel each other. Same behavior is found in ab-initio simulations by Mioshi et al. [18], where they found that copper atom clustering decreases rapidly above 400 K (here all simulation temperatures are close to the alloy solidus, above 860 K). This suggests that at higher temperatures (close to solidus), and at relatively low copper levels, the copper atoms interaction is mediated through their negative (compressive) lattice mismatch.

The same analysis was performed for all simulation cases listed in Table 3, which gave concurring results. The remaining data is shown in Supplementary material.

3.2.3. Crystal phases in rapid solidification

It is interesting to study the crystalline phases that form during rapid solidification. While FCC is the thermodynamically stable phase for pure aluminum and dilute Al–Cu, other configurations – such as BCC, HCP, and icosahedral short-range-ordered structure – are metastable

phases which can be kinetically favored in rapid solidification due to their smaller energy difference, and structural similarity, relative to the liquid, when compared to FCC [28,64].

Crystalline phases were detected using the Polyhedral Template Matching (PTM) algorithm implemented in OVITO [56]. The algorithm classifies the local structural environment of particles in the fully solidified system. PTM is generally more reliable than e.g., Common Neighbor Analysis (CNA) in the presence of strong thermal fluctuations and strains [56], which can be present in these rapid solidification simulations.

An example of the phase analysis is shown in Fig. 11, where a (100) oriented interface was solidified with $T_{nom} = 880$ K and $c_{nom} = 1$ at%Cu. During the solidification period, marked in gray background in Fig. 11a-d, the liquid domain was excluded by determining the solid–liquid interface location based on the order parameter (Section 2.4).

The simulations were continued for approximately 2 ns following the end of the solidification process to see how the phase fractions and their copper contents evolve over time. As the PTM-based raw phase fraction values fluctuate strongly over time (scatter points in Fig. 11a-d), a Savitzky–Golay smoothing filter was applied to the scatter data, shown as solid lines.

The results of the crystal phase classification are shown in Fig. 11, as well as the average copper concentrations in the respective phases. The phase 'Other' refers to unknown coordination structures, likely to be disordered or icosahedral short-range-ordered structures [28]. It is interesting to note that the phase fractions of "Other" and FCC, are approximately anticorrelated: this is likely because icosahedral short-range-ordered and disordered domains – which are in the region classified as solid according to the order parameter profile – are metastable configurations which are transforming towards the thermodynamically stable FCC structure. A similar metastable transition can be seen in HCP fraction, which first increases and start to decrease after approximately 2 ns. These trends are consistent with findings in Ref. [28].

It can be seen that HCP occurs at a higher solid fraction than BCC, which is consistent with Ref. [27], where using a MEAM potential for deeply quench polycrystalline pure aluminum, they detected HCP and not BCC as the minor solid phase. It is notable that the atoms classified as BCC and HCP are mostly isolated, as demonstrated in Fig. 11e. The cluster size distribution for each detected phase is shown in the Supplementary material.

Fig. 11 shows the evolution of the solute concentration in each crystal phase in the solidified domain, where it can be seen that copper content in all phases other than FCC are many times higher than the nominal composition (1 at.%Cu). Therefore, the presence of copper atoms is associated with a local change in crystal structure. This is consistent with earlier ab-initio simulations [17], where it is suggested that copper clustering is driven mainly by lattice relaxation in an aluminum matrix, leading to local deformation of the lattice and thereby a deviation from the typical FCC type crystal structure.

Fig. 12 shows the effect of copper content, as well as the quench depth, on the crystal phase fractions of (100)-oriented solidification simulations. This suggests that increasing the copper content increases the fraction of secondary metastable crystalline phases. This is consistent with the fact that copper concentration is higher in the secondary phases, as shown in Fig. 11. Furthermore, these results imply a stronger quench decreases the fraction of minor crystalline phases.

Intermetallic Al_2Cu-type ($\theta/\theta'/\theta''$) phase was not observed, similar to earlier rapid solidification Al–Cu MD simulations [26,28], although this potential is capable of properly forming Al_2Cu type phase [29]. Al_2Cu is absent because the system temperature should be lower to observe short-range ordering or decomposition into Al_2Cu type phases [17]. The topic of Al_2Cu formation in these rapid solidification structures is an interesting topic for future research.

For engineering application of rapid solidification (additively manufactured) precipitation-strengthened aluminum alloys, it would be interesting to further investigate the formation of pre-precipitates (or Guinier–Preston zones) related to Al_2Cu type phases in rapid solidification structures [17,65], including their propensity to form under rapid solidification crystal defects. However, these pre-precipitates require a drastic decrease of temperature to 600–700 K for dilute Al–Cu alloys to trigger a change in short-range ordering towards ordered precipitates [17]. It is also notable that these pre-precipitates might not have time to form during rapid solidification even if ambient temperatures are accessed but might require the simulation of a post-solidification heat treatments [3].

The subsequent evolution and growth of these pre-precipitates, during cool-down or annealing treatments, occur on longer (diffusive) time scales, require longer simulation times which might be challenging to reach with molecular dynamics simulations. For these cases, phase field crystal type models [66,67] or phase field models can become relevant.

3.3. Uncertainties in MD-extracted interfacial concentrations and temperature

In evaluating interfacial quantities from MD simulations (temperature, solid- and liquid-side concentrations), there is a general issue of accuracy versus statistical error. Interfacial quantities need to be measured on a sufficiently thin domain around the solid–liquid interface, while too thin domains lead to large statistical fluctuations in the measured quantities. The fluctuations can be decreased by increasing the system size (cross-sectional area normal to the solidification axis), which increases the computational costs. The error due to these fluctuations is shown as error bars in the $k - V$ (Fig. 3), as well as $T - V$ (Fig. 7) graph. On the other hand, there can be a systematic error related to choosing the width of the interfacial domains to properly represent the interfacial quantities. By considering multiple system cross section sizes (4.05×4.05 nm^2 vs. 8.1×8.1 nm^2 vs. 40.5×40.5 nm^2), we see a systematic decrease of random fluctuations in the interfacial quantities as the system size is increased. Most of the simulations are carried out for systems with an area of 8.1×8.1 nm^2, which in our opinion has a sufficiently small statistical error. The statistical error can also be decreased by running multiple simulations with an identical set-up (see e.g. Refs. [22,24]), but using different random seeds for the initialization.

As mentioned previously, in our experience, the method used in Ref. [22] resulted in partition coefficient values that are systematically lower than unity in the complete solute trapping regime; they used a separate scheme to decide whether complete trapping regime was reached (based on which they set $k = 1$). Therefore, it is possible that their method systematically underestimated the partition coefficient values below the complete trapping regime ($k < 1$). In Ref. [22], they calculated a time-average of the solute concentration profile and evaluated the solid- and liquid-side concentrations of this time-averaged profile. Conversely, we measured the instantaneous partition coefficient for each recorded time step and calculated the time-average of the instantaneous partition coefficients; this method leads to a partition coefficient that saturated to unity (within error bars) at complete trapping regime. We verified that complete trapping regime was indeed reached, by monitoring the binned solute concentration values $c(y)$ over time, whose change over time were negligible in the complete trapping regime.

The agreement between MD data and the interfacial temperature model $T(V)$ is rather good. It is to be noted that estimated interfacial temperatures are consistently higher than the thermostat temperature set in the simulation. Solidification leads to latent heat release around the solid–liquid interface, introducing thermal gradients in the system. While thermal gradients in solidification are physical as such, due to the absence of electronic contributions to heat conductivity, classical
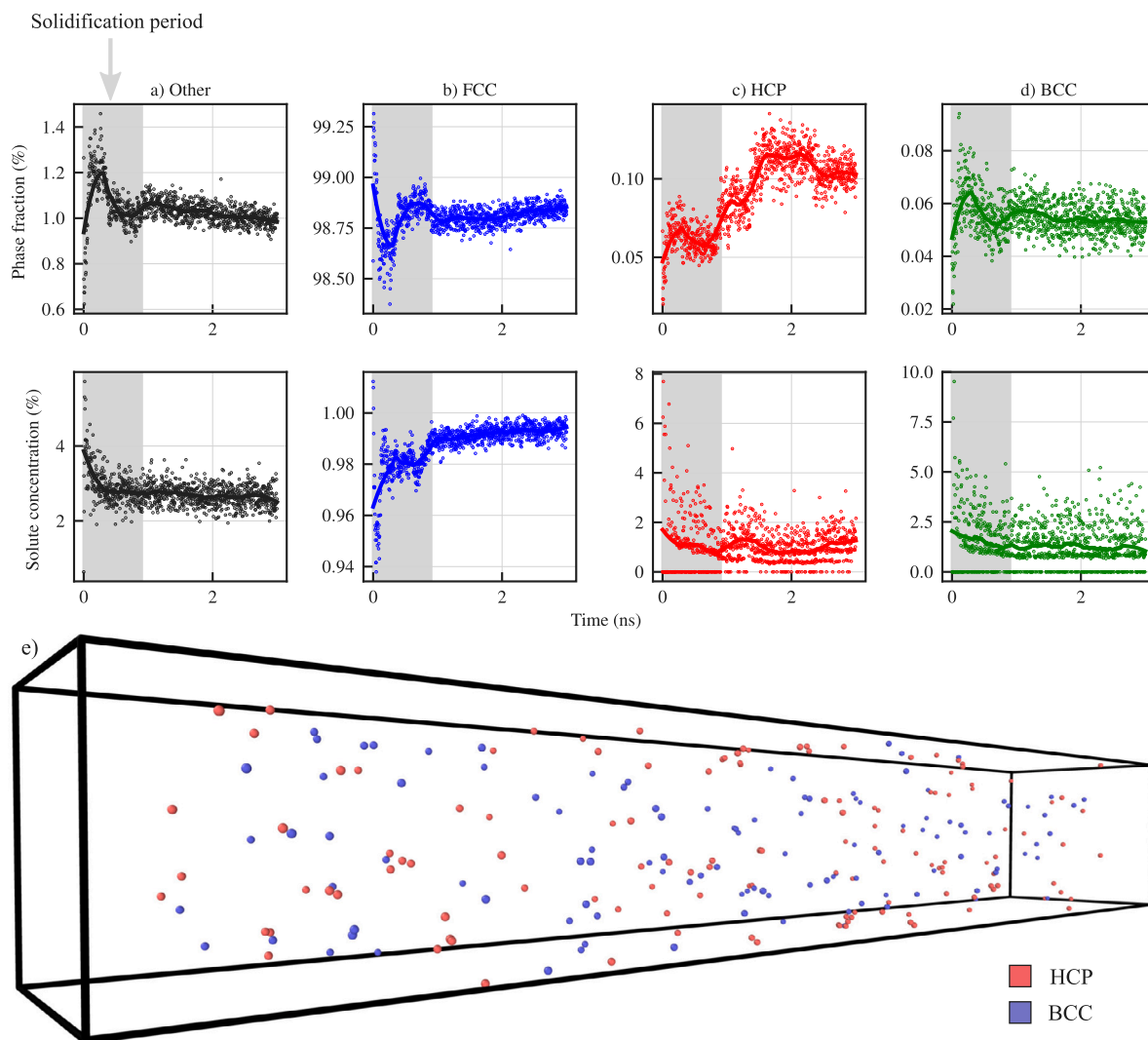
Fig. 11. The graphs show the phase fractions and their respective copper concentrations as a function of time, in the solidified domain (liquid domain excluded). The green area indicates the time interval before complete solidification. Dots show the data points, while the continuous line shows the smoothed evolution. Picture (e): atoms classified as HCP (red) and BCC (blue), taken at $t = 1.5$ ns, after the solidification is complete. Atoms near the y-boundaries (at distance less than 20 Å) are omitted, as the periodic boundary conditions result in unwanted interactions between the y-edges. Simulation parameters: $T_{nom} = 880$ K and $c_{nom} = 1$ at%Cu, yielding an average interfacial velocity of $V_{av} = 26.07$ m/s.

MD simulations of metals underestimate the magnitude of the thermal diffusivity [68]. One strategy to decrease the system heating and thermal gradients is to enforce a uniform target temperature in the system by dividing the full system into small subsystems with independent thermostats [68]. Therefore, while our decision to use a single global thermostat adds an "error bar" to the system temperature, we believe that this effect is sufficiently small and has a negligible effect on our findings.

4. Conclusion

In this paper, we performed rapid solidification of a dilute binary Al–Cu system using a quantum mechanics based analytical bond-order potential (BOP).

Firstly, we extracted the main solid–liquid interface properties controlling the solidification kinetics. Solid–liquid interface free energy and its anisotropy were measured in equilibrium simulations using the capillary fluctuation method. Additionally, non-equilibrium free solidification simulations were performed to obtain the kinetic coefficient and its anisotropy, as well as solute trapping parameters for Local Non-equilibrium (LNM) and Continuous Growth Model (CGM), including the solute drag coefficient. Kinetic coefficient results show good consistency in terms of the ratio μ_{100}/μ_{110} with proposed theoretical models and available MD simulation results. The aforementioned solid–liquid material parameters were found to be consistent with earlier MD simulations and experiments. These solid–liquid interface properties can be directly used as input parameters for example for quantitative phase field simulations of rapid solidification [69,70].

Secondly, we analyzed the rapid solidification structures. In addition to vacancies, we found significant number of interstitial defects. In the complete trapping regime, point defects formed as Frenkel defect pairs. The copper atoms were found to repel each other in these dilute alloy conditions, but copper was found to cluster around vacancies. In addition to FCC phase, small islands (mostly isolated atoms) of BCC and HCP phases were detected, where their stability was verified by proceeding the simulations after complete solidification. Compared to FCC, the BCC and HCP phases were accompanied by a local increase in copper content; the BCC and HCP fractions increased as the nominal copper content, as well as the quench depth, was increased.

These simulations provide insights into the rapid solidification structures that can help to develop and optimize heat-treatable aluminum alloys in terms of their composition and processing, including potential post-solidification heat treatments.
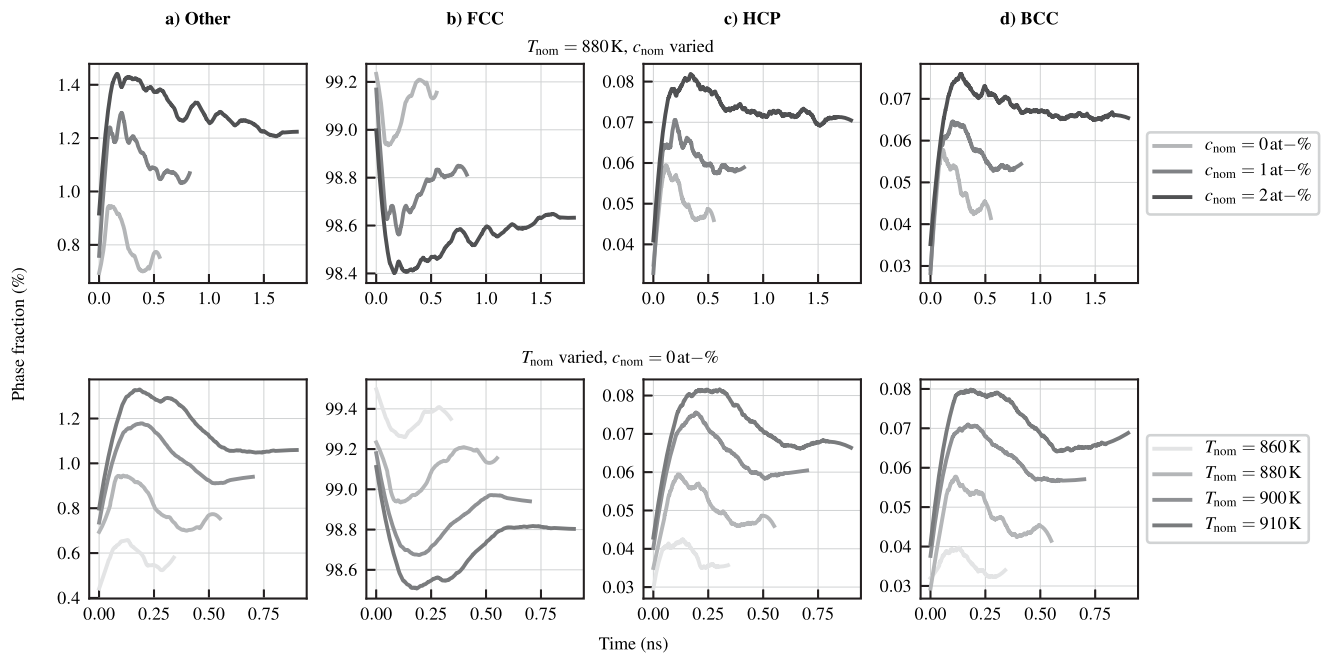
Fig. 12. Smoothed phase fractions as a function of time. Top row: the target quench temperature is kept constant ($T_{nom} = 880$ K), while the nominal solute concentration is varied. Bottom row: pure aluminum ($c_{nom} = 0$ at%Cu), while the target quench temperature is varied.

CRediT authorship contribution statement

Matias Haapalehto: Writing – original draft, Software, Visualization. **Tatu Pinomaa:** Supervision, Writing – review & editing. **Lei Wang:** Software, Methodology. **Anssi Laukkanen:** Supervision, Funding acquisition.

Declaration of competing interest

The authors declare that they have no known competing financial interests or personal relationships that could have appeared to influence the work reported in this paper.

Data availability

The raw/processed data required to reproduce these findings cannot be shared at this time due to technical or time limitations.

Acknowledgments

Appendix A. Supplementary data

Supplementary material related to this article can be found online at https://doi.org/10.1016/j.commatsci.2022.111356.

References

[1] E.J. Lavernia, T.S. Srivatsan, The rapid solidification processing of materials: science, principles, technology, advances, and applications, J. Mater. Sci. 45 (2) (2010) 287–325.
[2] S. David, S. Babu, J. Vitek, Welding: Solidification and microstructure, Jom 55 (6) (2003) 14–20.
[3] Y. Lin, S. Mao, Z. Yan, Y. Zhang, L. Wang, The enhanced microhardness in a rapidly solidified Al alloy, Mater. Sci. Eng. A 692 (2017) 182–191.
[4] Y. Ding, J. Muñiz-Lerma, M. Trask, S. Chou, A. Walker, M. Brochu, Microstructure and mechanical property considerations in additive manufacturing of aluminum alloys, MRS Bull. 41 (10) (2016) 745–751.
[5] T. DebRoy, H. Wei, J. Zuback, T. Mukherjee, J. Elmer, J. Milewski, A.M. Beese, A. Wilson-Heid, A. De, W. Zhang, Additive manufacturing of metallic components–process, structure and properties, Prog. Mater. Sci. 92 (2018) 112–224.
[6] H. Kotadia, G. Gibbons, A. Das, P. Howes, A review of laser powder bed fusion additive manufacturing of aluminium alloys: Microstructure and properties, Addit. Manuf. (2021) 102155.
[7] D.M. Herlach, Non-equilibrium solidification of undercooled metallic melts, Metals 4 (2) (2014) 196–234.
[8] J.W. Cahn, W.C. Carter, W.C. Johnson, The Selected Works of John W. Cahn, Wiley-TMS, 1998.
[9] M.J. Aziz, Interface attachment kinetics in alloy solidification, Metall. Mater. Trans. A 27 (3) (1996) 671–686.
[10] T. Pinomaa, A. Laukkanen, N. Provatas, Solute trapping in rapid solidification, MRS Bull. 45 (11) (2020) 910–915.
[11] R. Trivedi, W. Kurz, Solidification microstructures: A conceptual approach, Acta Metall. Mater. 42 (1994) 15.
[12] R.W. Balluffi, S.M. Allen, W.C. Carter, Kinetics of Materials, John Wiley & Sons, 2005.
[13] H.Y. Zhang, F. Liu, Y. Yang, D.Y. Sun, The molecular dynamics study of vacancy formation during solidifcation of pure metals, Sci. Rep. 7 (2017) 10241, http://dx.doi.org/10.1038/s41598-017-10662-x.
[14] A. Rukwied, A. Ruff, W. Willard, Study of the cellular solidification structure in a continuously cast high purity copper, Metall. Mater. Trans. B 2 (8) (1971) 2105–2114.
[15] Y.M. Wang, T. Voisin, J.T. McKeown, J. Ye, N.P. Calta, Z. Li, Z. Zeng, Y. Zhang, W. Chen, T.T. Roehling, et al., Additively manufactured hierarchical stainless steels with high strength and ductility, Nature Mater. 17 (1) (2018) 63.
[16] K. Bertsch, G.M. de Bellefon, B. Kuehl, D. Thoma, Origin of dislocation structures in an additively manufactured austenitic stainless steel 316L, Acta Mater. 199 (2020) 19–33.
[17] O. Gorbatov, A.Y. Stroev, Y.N. Gornostyrev, P. Korzhavyi, Effective cluster interactions and pre–precipitate morphology in binary Al-based alloys, Acta Mater. 179 (2019) 70–84.
[18] H. Miyoshi, H. Kimizuka, A. Ishii, S. Ogata, Temperature-dependent nucleation kinetics of Guinier-Preston zones in Al–Cu alloys: An atomistic kinetic Monte Carlo and classical nucleation theory approach, Acta Mater. 179 (2019) 262–272.
[19] I. Steinbach, Phase-field models in materials science, Modelling Simulation Mater. Sci. Eng. 17 (7) (2009) 073001.
[20] N. Provatas, K. Elder, Phase-Field Methods in Materials Science and Engineering, Wiley-VCH Verlag GmbH & Co. KGaA, 2010, http://dx.doi.org/10.1002/9783527631520.ch1.

[21] J. Rahman, Atomistic Simulations for Computing Solid Liquid Interface Properties of the Al-Mg System (Master's thesis), McMaster University, Canada, 2009.

[22] Y. Yang, H. Humadi, D. Buta, B.B. Laird, D. Sun, J.J. Hoyt, M. Asta, Atomistic simulations of nonequilibrium crystal-growth kinetics from alloy melts, Phys. Rev. Lett. 107 (2) (2011) 025505, http://dx.doi.org/10.1103/PhysRevLett.107.025505.

[23] S. Raman, J. Hoyt, P. Saidi, M. Asta, Molecular dynamics study of the thermodynamic and kinetic properties of the solid-liquid interface in FeMn, Comput. Mater. Sci. 182 (2020) 109773.

[24] S. Kavousi, B.R. Novak, J. Hoyt, D. Moldovan, Interface kinetics of rapid solidification of binary alloys by atomistic simulations: Application to Ti-Ni alloys, Comput. Mater. Sci. 184 (2020) 109854.

[25] Z. Sun, X. Tan, S.B. Tor, C.K. Chua, Simultaneously enhanced strength and ductility for 3D-printed stainless steel 316L by selective laser melting, NPG Asia Mater. (2018) 1.

[26] A. Mahata, M.A. Zaeem, Effects of solidification defects on nanoscale mechanical properties of rapid directionally solidified Al-Cu alloy: A large scale molecular dynamics study, J. Cryst. Growth 527 (2019) 125255.

[27] A. Mahata, M.A. Zaeem, Evolution of solidification defects in deformation of nano-polycrystalline aluminum, Comput. Mater. Sci. 163 (2019) 176–185.

[28] Q. Zhang, J. Li, S. Tang, Z. Wang, J. Wang, Atomistic mechanism underlying nucleation in Al–Cu alloys with different compositions and cooling rates, J. Phys. Chem. C 125 (6) (2021) 3480–3494.

[29] X. Zhou, D. Ward, M. Foster, An analytical bond-order potential for the aluminum copper binary system, J. Alloys Compd. (ISSN: 0925-8388) 680 (2016) 752–767, http://dx.doi.org/10.1016/j.jallcom.2016.04.055.

[30] S. Plimpton, Fast parallel algorithms for short-range molecular dynamics, J. Comput. Phys. 117 (1) (1995) 1–19.

[31] H. Ramalingam, M. Asta, A. van de Walle, J.J. Hoyt, Atomic-scale simulation study of equilibrium solute adsorption at alloy solid-liquid interfaces, Interface Sci. 10 (2002) 149–158, http://dx.doi.org/10.1023/A:1015889313170.

[32] J. Hoyt, M. Asta, A. Karma, Method for computing the anisotropy of the solid-liquid interfacial free energy, Phys. Rev. Lett. 86 (24) (2001) 5530, http://dx.doi.org/10.1103/PhysRevLett.86.5530.

[33] A. Savitzky, M.J.E. Golay, Smoothing and differentiation of data by simplified least squares procedures, Anal. Chem. 36 (8) (1964) 1627–1639, http://dx.doi.org/10.1021/ac60214a047.

[34] M.J. Aziz, T. Kaplan, Continuous growth model for interface motion during alloy solidification, Acta Metall. 36 (1988) 2335.

[35] S. Sobolev, Rapid solidification under local nonequilibrium conditions, Phys. Rev. E 55 (6) (1997) 6845.

[36] D.S. Ivanov, L.V. Zhigilei, Combined atomistic-continuum modeling of short-pulse laser melting and disintegration of metal films, Phys. Rev. B 68 (6) (2003) 064114.

[37] R. Trivedi, W. Kurz, Dendritic growth, Int. Mater. Rev. 39 (2) (1994) 49–74.

[38] C.A. Becker, D.L. Olmsted, M. Asta, J.J. Hoyt, M. Foiles, Atomistic simulations of crystal-melt interfaces in a model binary alloy: Interfacial free energies, adsorption coefficients, and excess entropy, Phys. Rev. B 79 (2009) 054109, http://dx.doi.org/10.1103/PhysRevB.79.054109.

[39] F. Spaepen, A structural model for the solid-liquid interface in monatomic systems, Acta Metall. (ISSN: 0001-6160) 23 (6) (1975) 729–743, http://dx.doi.org/10.1016/0001-6160(75)90056-5.

[40] J. Hoyt, S. Raman, N. Ma, M. Asta, Unusual temperature dependence of the solid-liquid interfacial free energy in the Cu-Zr system, Comput. Mater. Sci. (ISSN: 0927-0256) 154 (2018) 303–308, http://dx.doi.org/10.1016/j.commatsci.2018.07.050.

[41] L. Wang, J.J. Hoyt, N. Wang, N. Provatas, C.W. Sinclair, Controlling solid-liquid interfacial energy anisotropy through the isotropic liquid, Nature Commun. 11 (1) (2020) 1–7.

[42] T. Frolov, Y. Mishin, Solid-liquid interface free energy in binary systems: Theory and atomistic calculations for the (110) Cu–Ag interface, J. Chem. Phys. 131 (5) (2009) 054702, http://dx.doi.org/10.1063/1.3197005.

[43] E. Asadi, M. Asle Zaeem, S. Nouranian, M.I. Baskes, Two-phase solid–liquid coexistence of Ni, Cu, and Al by molecular dynamics simulations using the modified embedded-atom method, Acta Mater. 86 (2015) 169–181, http://dx.doi.org/10.1016/j.actamat.2014.12.010.

[44] J. Morris, Z. Lu, Y. Ye, K. Ho, The anisotropic free energy of the solid-liquid phase boundary in Al, Interface Sci. 10 (2002) 143–148, http://dx.doi.org/10.1023/A:1015800629100.

[45] J.J. Hoyt, M. Asta, A. Karma, Atomistic and continuum modeling of dendritic solidification, Mater. Sci. Eng. R 41 (6) (2003) 121–163.

[46] L. Gránásy, M. Tegze, A. Ludwig, Solid–liquid interfacial free energy, in: H. Fredriksson, S. Savage (Eds.), Rapidly Quenched Materials, Elsevier, Oxford, 1991, pp. 577–580, http://dx.doi.org/10.1016/B978-0-444-89107-5.50140-4.

[47] M. Gündüz, J. Hunt, The measurement of solid-liquid surface energies in the Al–Cu, Al–Si and Pb–Sn systems, Acta Metall. 33 (9) (1985) 1651–1672, http://dx.doi.org/10.1016/0001-6160(85)90161-0.

[48] Q. Jiang, H. Lu, Size dependent interface energy and its applications, Surf. Sci. Rep. 63 (10) (2008) 427–464, http://dx.doi.org/10.1016/j.surfrep.2008.07.001.

[49] S. Liu, R. Napolitano, R. Trivedi, Measurement of anisotropy of crystal-melt interfacial energy for a binary Al—Cu alloy, Acta Mater. 49 (20) (2001) 4271–4276, http://dx.doi.org/10.1016/S1359-6454(01)00306-8.

[50] P.M. Smith, M.J. Aziz, Solute trapping in aluminum alloys, Acta Metall. 42 (1994) 3515–3525.

[51] M.I. Mendelev, M.J. Rahman, J.J. Hoyt, M. Asta, Molecular-dynamics study of solid–liquid interface migration in fcc metals, Modelling Simulation Mater. Sci. Eng. 18 (7) (2010) 074002, http://dx.doi.org/10.1088/0965-0393/18/7/074002.

[52] M.I. Mendelev, F. Zhang, H. Song, Y. Sun, C.Z. Wang, K.M. Ho, Molecular dynamics simulation of the solid-liquid interface migration in terbium, J. Chem. Phys. 148 (21) (2018) 214705, http://dx.doi.org/10.1063/1.5026922.

[53] F. Celestini, J.-M. Debierre, Measuring kinetic coefficients by molecular dynamics simulation of zone melting, Phys. Rev. E 65 (2002) 041605, http://dx.doi.org/10.1103/PhysRevE.65.041605.

[54] J.J. Hoyt, M. Asta, Atomistic computation of liquid diffusivity, solid-liquid interfacial free energy, and kinetic coefficient in Au and Ag, Phys. Rev. B 65 (2002) 214106, http://dx.doi.org/10.1103/PhysRevB.65.214106.

[55] S. Blairs, Sound velocity of liquid metals and metalloids at the melting temperature, Phys. Chem. Liq. 45 (4) (2007) 399–407.

[56] A. Stukowski, Visualization and analysis of atomistic simulation data with OVITO-the open visualization tool, Model. Simul. Mater. Sci. Eng. 18 (1) (2010) http://dx.doi.org/10.1088/0965-0393/18/1/015012.

[57] K. Nordlund, R. Averback, Role of self-interstitial atoms on the high temperature properties of metals, Phys. Rev. Lett. 80 (19) (1998) 4201.

[58] Y. Ashkenazy, R. Averback, Atomic mechanisms controlling crystallization behaviour in metals at deep undercoolings, Europhys. Lett. 79 (2) (2007) 26005.

[59] C. Gordon, A. Granato, Equilibrium concentration of interstitials in aluminum just below the melting temperature, Mater. Sci. Eng. A 370 (1–2) (2004) 83–87.

[60] E. Safonova, Y.P. Mitrofanov, R. Konchakov, A.Y. Vinogradov, N. Kobelev, V. Khonik, Experimental evidence for thermal generation of interstitials in a metallic crystal near the melting temperature, J. Phys.: Condens. Matter 28 (21) (2016) 215401.

[61] D. Ward, X. Zhou, R. Karnesky, R. Kolasinski, M. Foster, R. Sills, K. Thürmer, P. Chao, E. Epperly, B. Wong, et al., Understanding H Isotope Adsorption and Absorption of Al-Alloys Using Modeling and Experiments, SAND2015-8388, Sandia National Laboratories, 2015.

[62] B. Jelinek, S. Groh, M.F. Horstemeyer, J. Houze, S.-G. Kim, G.J. Wagner, A. Moitra, M.I. Baskes, Modified embedded atom method potential for Al, Si, Mg, Cu, and Fe alloys, Phys. Rev. B 85 (24) (2012) 245102.

[63] M. Hillert, M. Schwind, M. Selleby, Trapping of vacancies by rapid solidification, Acta Mater. 50 (12) (2002) 3285–3293.

[64] S. An, R. Su, Y.-C. Hu, J. Liu, Y. Yang, B. Liu, P. Guan, Common mechanism for controlling polymorph selection during crystallization in supercooled metallic liquids, Acta Mater. 161 (2018) 367–373.

[65] K. Zweiacker, C. Liu, M. Gordillo, J. McKeown, G. Campbell, J. Wiezorek, Composition and automated crystal orientation mapping of rapid solidification products in hypoeutectic Al-4 at.% Cu alloys, Acta Mater. 145 (2018) 71–83.

[66] G. Kocher, N. Provatas, Thermodensity coupling in phase-field-crystal-type models for the study of rapid crystallization, Phys. Rev. Mater. 3 (2019) 053804.

[67] X. Shuai, Z. Wang, H. Mao, S. Tang, Y. Kong, Y. Du, Atomic-scale study of compositional and structural evolution of early-stage grain boundary precipitation in Al–Cu alloys through phase-field crystal simulation, J. Mater. Sci. 56 (22) (2021) 12700–12715.

[68] J. Monk, Y. Yang, M.I. Mendelev, M. Asta, J.J. Hoyt, D.Y. Sun, Determination of the crystal-melt interface kinetic coefficient from molecular dynamics simulations, Model. Simul. Mater. Sci. Eng. 18 (2009) 015004.

[69] T. Pinomaa, N. Provatas, Quantitative phase field modeling of solute trapping and continuous growth kinetics in quasi-rapid solidification, Acta Mater. 168 (2019) 167–177.

[70] S. Kavousi, B.R. Novak, D. Moldovan, M.A. Zaeem, Quantitative prediction of rapid solidification by integrated atomistic and phase-field modeling, Acta Mater. 211 (2021) 116885.